Chapter 8
Application: Detonations

Detonation is a shock-induced combustion in which chemical reactions are closely coupled with shock waves. The shock wave compresses the reactant with an abrupt increase in temperature and pressure, initiating the reactants to be burnt into products. The intense heat release permits the high propagating speed of the shock wave to be sustained. It is fundamental research related to both the safety industry and propulsion systems. For most explosive mixtures, detonation wave speeds are formulated by Chapman–Jouguet (CJ) theory. Typical detonation velocities for gaseous mixtures generally range from 1400 to 3000 m/s. Behind the shock, the time scale for reactions is commonly on the order of microseconds or even less. Furthermore, the detonation front is intrinsically unstable, forming transient multi-dimensional structures. Many studies revealed that high resolution is necessary to resolve the essential detonation structures. Due to its complex nature and multiple time scales, detonation is thus a challenging problem for solvers on shock-capturing capability, robustness, and computational efficiency. This chapter will present several essential aspects of detonation research by applying the CESE schemes.

8.1 Gaseous Detonations

In detonation simulations, the requirement for the computational resources is usually very high because the satisfactory resolution is necessary to compute the coupling between flow and chemical reactions and to resolve the detonation structures. As a result, applying detailed chemistry is usually limited to problems with simple and small domains or particular situations. Otherwise, simulations with simplified models are preferred to gain insight into the physics without loss of credibility. For illustrative purposes, we consider a system for ideal gas and a simplified chemical model. The 2D inviscid reactive compressible flow equations can be expressed as

$$\frac{\partial \boldsymbol{U}}{\partial t} + \frac{\partial \boldsymbol{F}}{\partial x} + \frac{\partial \boldsymbol{G}}{\partial y} = \boldsymbol{S} \tag{8.1}$$

where the conserved variable vector $\boldsymbol{U}$, the flux vectors $\boldsymbol{F}$, $\boldsymbol{G}$ and source term vector $\boldsymbol{S}$ are defined as $\boldsymbol{U} = [\rho,\, \rho u,\, \rho v,\, E,\, \rho\lambda]^T$, $\boldsymbol{F} = [\rho u,\, \rho u^2 + p,\, \rho uv,\, (E + p)u,\, \rho\lambda u]^T$, $\boldsymbol{G} = [\rho v,\, \rho uv,\, \rho v^2 + p,\, (E + p)v,\, \rho\lambda v]^T$, $\boldsymbol{S} = [0,\ 0,\ 0,\ 0,\ \dot{\omega}]^T$. The symbols ρ, u, v, p, E, and λ denote density, velocities in x and y directions, pressure, the total energy per unit volume, and mass fraction of the reactant, respectively. The perfect gas law was adopted here as $p = \rho RT$, where R is the gas constant and T is the gas temperature. The total energy is

$$E = \frac{p}{(\gamma - 1)} + \frac{1}{2}\rho(u^2 + v^2) + \rho\lambda Q, \tag{8.2}$$

where γ and Q are the specific heat ratio and the specific heat release. The chemical reaction rate is formulated by the one-step Arrhenius model as

$$\dot{\omega} = -k\rho\lambda e^{-E_a/RT}, \tag{8.3}$$

where k is the pre-exponential factor, and E_a denotes the activation energy.

8.1.1 Ignition of Detonations

Ignition of detonation refers to the formation of a detonation wave through either an instantaneous onset or the transition from deflagration. Shen and Parsani [1] studied the direct ignition of spherical detonation by using the upwind CESE scheme to solve Eq. (8.1). The distance between the shock wave and the position where half of the reactant is consumed can be defined as the half-reaction length. A uniform resolution with 20 meshes per half-reaction length was adopted, and the number of mesh points is 1.6 billion. It is well-known that the dynamics of detonation are sensitive to the activation energy. Thus, three activation energies representing stable ($E_a = 15$), mildly unstable ($E_a = 27$), and highly unstable ($E_a = 50$) detonations were studied. For different E_a, k was adjusted to fix the half-reaction length in unit length. A hot spot with $p_s = (\gamma - 1)E_s$, $T_s = 20.0$, and a radius of 1 was used to form a blast wave to ignite the mixture. All variables above are nondimensionalized with respect to the state of the unburnt reactant.

The peak pressure history behind the shock for 1D detonations are depicted in Fig. 8.1, and typical 2D contours are plotted in Fig. 8.2. For stable case (Fig. 8.1a), the subcritical, critical, and supercritical regimes are observed successively when E_s increases from 1.8×10^4 to 1.0×10^5. In the critical regime, $E_s = 2.0 \times 10^4$ (Fig. 8.1b), P_{sh} first decays and then rapidly increases due to the formation and amplification of the pressure pulse behind the leading shock. The 2D result shows a
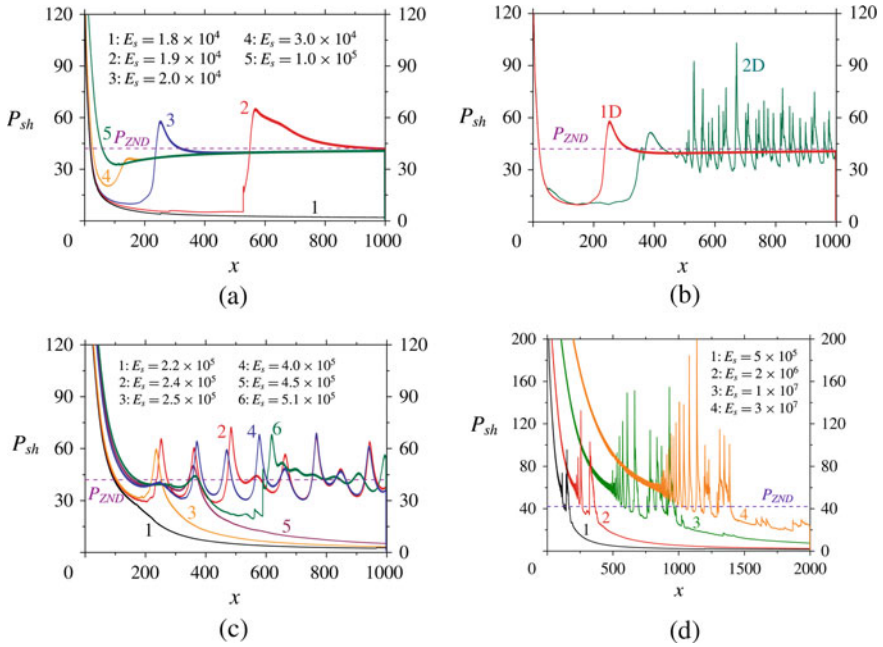
Fig. 8.1 Peak pressure history at the shock front (P_{sh}) as a function of position and source energy (E_s), for **a** $E_a = 15$, **b** $E_a = 15$, $E_s = 2 \times 10^4$, **c** $E_a = 27$, **d** $E_a = 50$. Courtesy of H. Shen [1]

highly oscillatory pattern for P_{sh} due to the development of multidimensional instabilities, and the run-up distance deviates from 1D solution. Three critical energies were detected for the mildly unstable case (Fig. 8.1c), The authors further observed the fourth critical energy when refining the search using a minor incremental E_s. However, there might be a unique critical energy in the 2D case. The inconsistency between 1 and 2D becomes more apparent for the highly unstable cases. For all the E_s tested, 1D detonation eventually failed (Fig. 8.1d). The results suggest that, without large overdriven, the 1D detonation propagation through auto-ignition is impossible for the highly unstable cases. Contrarily, the critical energy is approximately 1.5×10^5 for 2D cases (Fig. 8.2d). The key factors dominating the direct ignition of 2D detonation are the unsteadiness arising from the decay of the leading shock, heat release from the chemical reaction, and the inherent multidimensional instabilities. In 1D detonations, only the first two aforementioned factors exist. Detonation fails when the excessive unsteadiness overtakes the heat release. The transverse waves induced by the multidimensional instabilities create local over-driven detonations. On the one hand, these local over-driven detonations facilitate the propagation of the global detonation; on the other hand, induce stronger expansion waves to increase the risk of failure. The competition among these three factors should be considered to provide a comprehensive model of direct initiations.
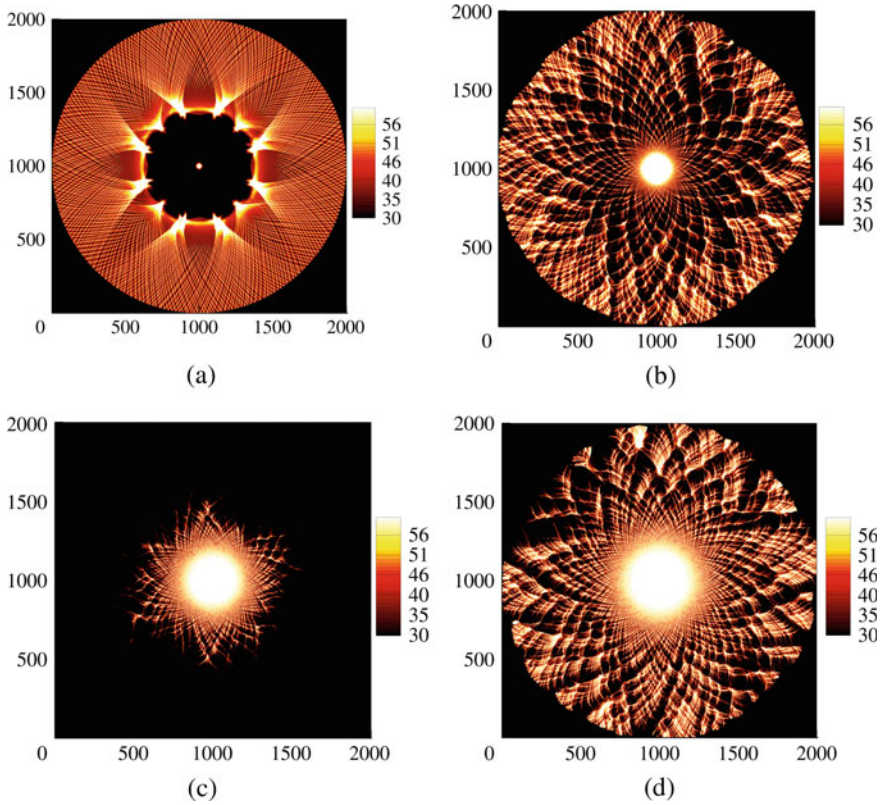
Fig. 8.2 Maximum pressure history in two dimensions. **a** $E_a = 15$, $E_s = 2.5 \times 10^4$, **b** $E_a = 27$, $E_s = 4.5 \times 10^4$, **c** $E_a = 50$, $E_s = 1.0 \times 10^4$, **d** $E_a = 50$, $E_s = 1.5 \times 10^4$. Courtesy of H. Shen [1]

Another situation of detonation ignition occurs when the gaseous reactant in the unconfined space is ignited through the detonation wave emerging from a small tube. When the detonation wave diffracts from a tube into the unconfined space, the substantial expansion will perturb the detonation front. If tube size is small enough, the detonation wave will quench (subcritical), otherwise, the detonation will continue to propagate (supercritical). Shi et al. [2] investigated the 2D detonation diffraction using the a–α CESE scheme. Two scenarios were considered. If the detonation wave inside the tube does not contain transverse waves, it is classified as the planar case. Otherwise, it is classified as the cellular case. In these simulations, Eqs. (8.1)–(8.3) were employed with $E_a = 24$ to assure that 1D detonation wave is stable (For E_a higher than 25.27, 1D detonation is intrinsically unstable). A resolution with 24 meshes per half-reaction length was tested converged for current settings, and the total mesh points are around 410 million. A first glance at the results revealed that the critical channel width for cellular scenarios is smaller than that for the planar case (Table 8.1). Four cases, including supercritical and subcritical for planar and cellular

Table 8.1 Critical channel width for $E_a = 24$

	Lower limit	Upper limit
Planar	100	110
Cellular	75	85

scenarios, were carefully discussed by examining wave structures and Lagrangian particles that are initially scattered in the flow.

For planar scenarios, the disturbance originates from the corner propagates towards the symmetric line. The diffracted shock wave decelerates and decouples with the flame front. In the shocked reactant, a compression wave is formed and amplified through the temperature gradient towards the leading shock. The compression wave is indicated by the successive abrupt change in temperature for particles E7–E9 (Fig. 8.3). When this compression wave merges with the leading shock, detonation may be facilitated if the strengthened shock wave exceeds a critical value. On the other hand, the aforementioned disturbance reflects from the symmetric line, and the reflected rarefaction (Fig. 8.4) wave may simultaneously affect the shocked reactant and hinder the formation and amplification of the compression wave. For the sub-critical case, i.e., $w = 100$, re-initiation is reproduced if the boundary condition is modified such that the rarefaction wave does not reflect towards the leading shock. Therefore, for the planar cases, re-initiation is attributed to the competition between the coalescence of the amplified compression wave with the leading shock and the strength of the reflected rarefaction wave.

For cellular scenarios, the re-initiation patterns are different from the planar cases. Despite the number of transverse waves decreases when the detonation wave expands into the unconfined space. It is interesting to note that from Fig. 8.5, a complete decoupling is not observed during the propagation of the supercritical case ($w = 85$) (a complete decouple is observed before re-initiation in the planar $w = 110$
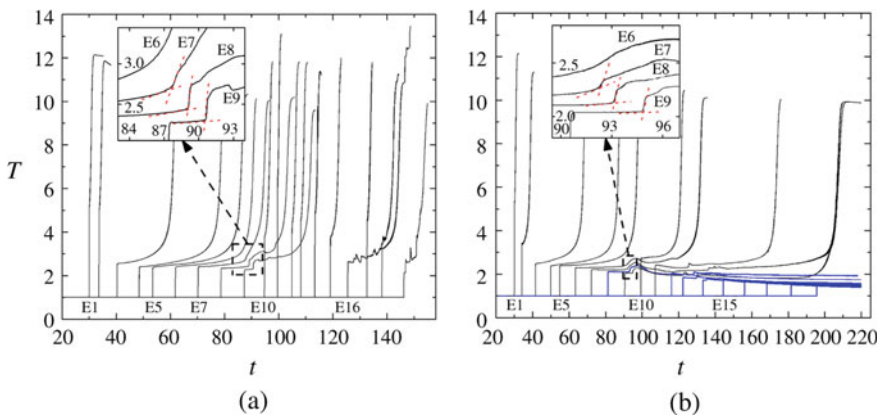

Fig. 8.3 Temperature traces of particles along the re-initiation direction for planar detonation diffraction: **a** $w = 110$ and **b** $w = 100$. Courtesy of L. S. Shi [2]
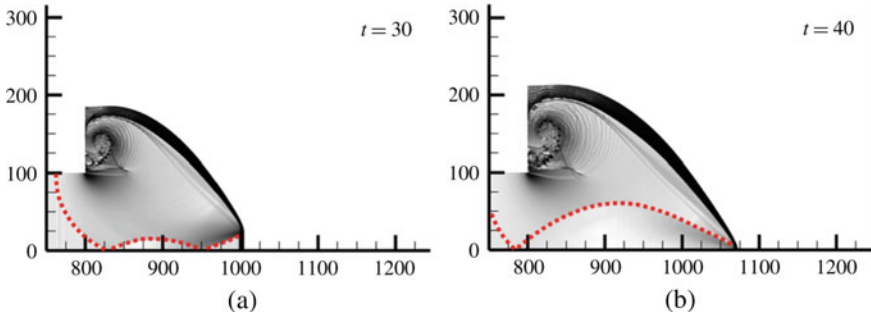
Fig. 8.4 Numerical schlieren images for planar case with $w = 100$. Red dash lines indicated the head of rarefaction. Courtesy of L. S. Shi [2]
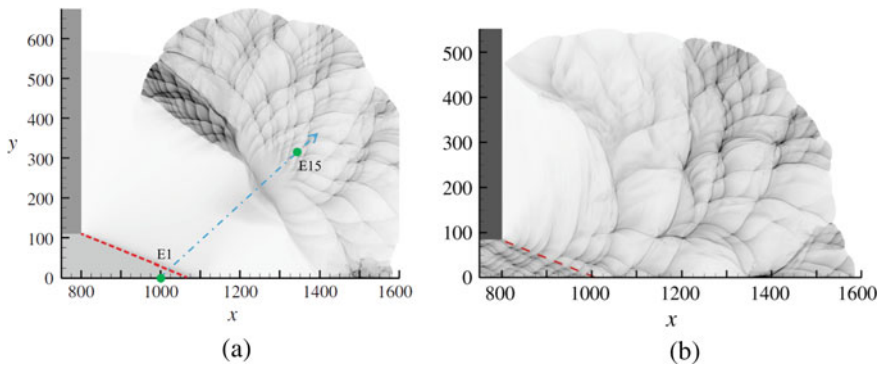

Fig. 8.5 Numerical soot foils for **a** planar detonation diffractions, $w = 110$, **b** cellular detonation diffractions, $w = 85$. The red dashed lines indicate the disturbance line predicted by Skews' model. The blue dash-dot line is the re-initiation path along which particles E_i are initially located. Courtesy of L. S. Shi [2]

case). Detonation wave sustains through the continuous formation of local overdriven detonation when transverse waves collide. Previous experimental research revealed that the critical tube diameter for unstable mixtures is $d_c \approx 13\lambda$ (λ: detonation cell size), but $d_c \approx 30\lambda$ or even more were measured for stable mixtures highly diluted with argon. The distinct difference between the re-initiation mechanisms planar and cellular detonation diffractions elaborated in current simulation provides a plausible explanation of the discrepancy of the correlations on critical tube sizes. In unstable detonations, where the formation of local hot spots is essential to sustain the detonation, the correlation between the d_c and λ is established. It is well-known that the cellular patterns in stable detonation are regular, with transverse wave velocity approximately being the sound velocity in the burned products. This corresponds to the planar scenarios. Detonation re-initiates if the influence of the reflected rarefaction wave is negligible. Thus the d_c / λ correlation may not be necessary.

8.1.2 Dynamics of Detonations

As discussed in Sect. 8.1, multi-dimensional instability is a fundamental phenomenon in detonation. In this section, we will elaborate more on the studies on detonation propagation in one, two, and three dimensions using CESE schemes.

Wang et al. [3] have implemented 2D CESE on detonation reflection on a wedge using a detailed reaction model. Later, in the study on the propagation modes of stoichiometric H_2/O_2 3D cellular detonation in a square duct [4], two types of propagation modes were verified, which depended on the configuration of the initial conditions. Unreacted pockets with complex structures were also captured by using the improved CESE scheme.

Numerous numerical studies based on detailed chemical mechanisms have quantitatively reproduced the key structures of multi-dimensional detonations. They experienced barriers to predict the cell size correctly. For example, for H_2/O_2 mixture highly diluted by argon, the regular cell sizes predicted from simulation using detailed chemical mechanisms were approximately half of those measured in experiments. One of the important physical phenomena in high-speed flow, the vibrational non-equilibrium of molecules, was usually ignored in early numerical studies. Behind the detonation wave, the time scales for vibrational relaxation and chemical reaction are comparable. Shi et al. [5] re-examined this problem with the consideration of vibrational relaxation and its coupling with reactions. The convection of vibrational energy was integrated into governing equations, and the translational-rotational energy and the vibrational energy were separated in the formulation of the total energy, which is composed of enthalpy of formation, translational-rotational energy, kinetic energy, and vibrational energy. The energy exchange rate was calculated by the Landau-Teller model.

Four scenarios were compared in 1D and 2D simulations. (1) The mixture is assumed to be thermodynamically equilibrium. (2) Vibrational relaxation is incorporated, and the translational temperature is kept as the dominant temperature of the chemical reactions. (3) Vibrational relaxation is considered, and the geometric average temperature is used to compute the reaction rates. (4) The physically consistent vibration-chemistry-vibration coupling model is adopted to account for the effect of vibrational non-equilibrium on chemical reaction rates. Examples of 1D detonation structures are depicted in Fig. 8.6. Model (2) exhibits a temperature overshot behind the shock compared to the equilibrium case because the mixture remains vibrational cold. The vibrational temperature approaches the equilibrium state gradually, and a noticeable disparity still exists when exothermic reactions are triggered. Since translational-rotational temperature controls reactions in model (2), the overshot in temperature results in a marginal decrease in the half-reaction length (δ). In model (3), the geometric averaged temperature is used to calculate the reaction rate. The onset of severe chemical reactions occurs only when the vibrational relaxation approaches equilibrium. The half-reaction length increases by 1.64 times that in the model (1). A similar trend is observed in the case using model (4). The detonation
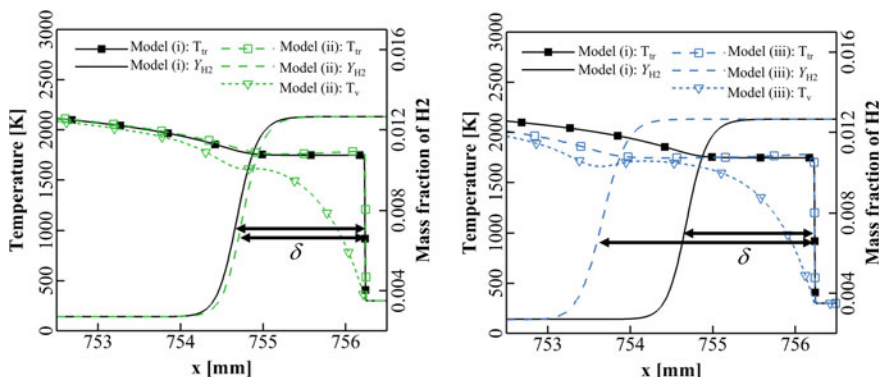
Fig. 8.6 Temperature and H$_2$ distribution with initial condition of 0.1 atm and 300 K. Left: scenarios 1 and 2. Right: scenarios 1 and 3. Courtesy of L. S. Shi [5]

cell widths are predicted from 2D simulation using models (1) and (2) are approximately the same. The cell widths using models (3) and (4) are approximately 1.32 and 1.34 times the value of that in the model (1). It reveals that the vibrational-chemical coupling effect may be one of the factors responsible for the failure to correctly predict the cell size.

Later, Uy et al. [6] further examine the effect of vibrational non-equilibrium on the one-dimensional instabilities using the CESE scheme. In this study, 1D piston-supported detonation case with fixed non-dimensional specific heat release $Q = 50$, the ratio of specific heats $\gamma = 1.2$, and characteristic vibrational temperature $\theta = 20$. The ratio between the chemical time scale τ_c and the vibrational time scale τ_V was selected as a control parameter. Park's two-temperature model was used to evaluate the effect of vibrational non-equilibrium on the chemical reaction rate. The neutral stability limit under the vibrational equilibrium assumption is approximately $E_a = 26.47$, above which the detonation is unstable with amplified oscillation. Numerical tests reveal $E_a = 27$ with the thermal equilibrium assumption being longitudinally unstable. Nevertheless, for finite vibrational relaxation rate (i.e., the $\tau^\alpha \equiv \tau_c/\tau_V \neq \infty$), the amplitudes of pressure oscillations decay for smaller $\tau^\alpha = 3, 5, 7$, and the oscillation decays much faster for as τ^α decreases. The results imply that the propagation of detonation is stabilized because of the vibrational non-equilibrium. Theoretical analysis using linear stability analysis (LSA) under different overdriven factors $f = (D/D_{CJ})^2$ was also provided in Uy et al. [7]. The neutral stability limit predicted using the CESE scheme agrees very well with LSA (Table 8.2). The accuracy of CESE in solving detonation problems is further confirmed.

Table 8.2 Comparison of the neutral stability limit (NSL) and the period of oscillation (PO) computed by LSA and numerical simulation. Case I: $f = 1$, thermal equilibrium (eq). Case II: $f = 1$, thermal nonequilibrium (neq), $\tau^\alpha = 5$. Case III: $f = 1$, neq, $\tau^\alpha = 7$. Case IV: $f = 1$, neq, $\tau^\alpha = 9$. Case V: $E_a = 50$, eq. Case VI: $E_a = 50$, neq, $\tau^\alpha = 5$. Case VII: $E_a = 50$, neq, $\tau^\alpha = 10$. Case VIII: Ea = 50, neq, $\tau^\alpha = 20$. Courtesy of C. K. Uy [7]

Case	Linear stability analysis		Numerical simulation	
	NSL	PO	NSL	PO
I	$E_a = 26.46$	10.63	$E_a = 26.47$	10.64
II	$E_a = 27.13$	12.14	$E_a = 27.14$	12.15
III	$E_a = 26.99$	11.77	$E_a = 27.02$	11.74
IV	$E_a = 26.90$	11.54	$E_a = 26.92$	11.51
V	$f = 1.62$	8.02	$f = 1.62$	8.03
VI	$f = 1.555$	9.51	$f = 1.554$	9.52
VII	$f = 1.582$	8.80	$f = 1.581$	8.83
VIII	$f = 1.60$	8.46	$f = 1.598$	8.43

8.1.3 Rotating Detonation Waves

Because of the rapid compression of the mixture and the quasi-constant volume combustion, the high thermodynamic efficiency of detonation makes it favourable to be employed in developing potential detonation engines. The rotating detonation engine (RDE) is one of the promising candidates in which the detonation wave propagates circumferentially, and the reactant is continuously injected into the combustion chamber.

Figure 8.7 depicts the flow features of RDE simulated with the upwind CESE schemes. The 2D simulation is essentially the unwrapped RDE channel from a 3D geometry. The top is the RDE outlet described by a non-reflective boundary. The reactant is injected into the combustor from the bottom through micro-Laval nozzles. The ideal injection was assumed that all the bottom areas could inject fresh reactant. Typical flow features of RDE can be observed, characterized by a rotating detonation wave, triangular reactant layer, oblique shock, and slip line. Furthermore, Wang et al. [8] used an improved CNI 2D CESE scheme to study the kerosene/air RDE. The results suggested that decreasing the inlet/wall ratio would reduce the strength of the detonation wave, and the reaction zone would be elongated. With further decreasing the air ratio, the burned gas emerges in the triangular zone, and the detonation wave fails to be self-sustained.
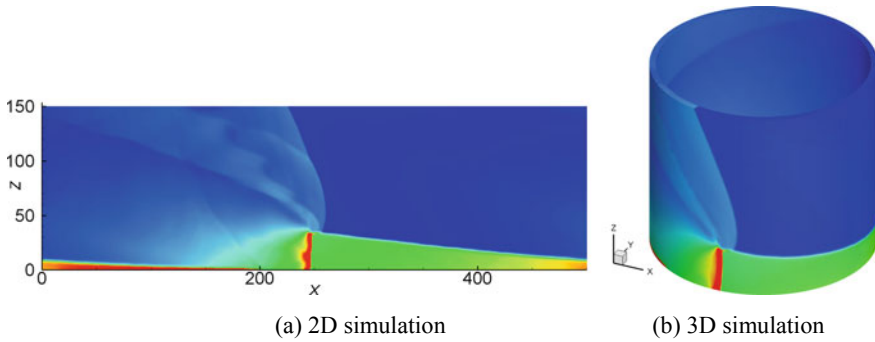
(a) 2D simulation   (b) 3D simulation

Fig. 8.7 Density contours of 2D and 3D RDE simulations using the upwind CESE scheme

8.2 Two-Phase Detonations

Liquid fuels and energetic powders are of advantages of high energy density and easy storage, which makes them common in practical propulsion systems. Detonation-based propulsion systems using these non-gaseous fuels involve reactive multi-phase high-speed flows. Although gaseous, liquid and/or solid phases are involved in these detonation phenomena, it is always referred to as two-phase detonation from the viewpoint of reactants, namely gas–liquid two-phase detonation and gas–solid two-phase detonation. Compared to gaseous detonations, two-phase detonations are characterized not only by shock waves and fast combustion, but also by multi-phase interaction and multi-scales, leading to great difficulties in numerical simulations. With the successful applications of the CESE method in gaseous detonation simulations, it is imperative to extend the CESE method to two-phase detonation problems and test its capabilities of accuracy and robustness in two-phase detonation simulations.

There are mainly two kinds of frameworks that are used to address the discrete phase in two-phase detonation simulations, namely the Eulerian–Eulerian framework and the Eulerian–Lagrangian framework. Between these two frameworks, the Eulerian–Eulerian framework, which is also referred to as the two-fluid model/method, is more common and easier in implementation and extension in two-phase detonation simulations. The discrete phase (the liquid phase in gas–liquid two-phase detonations or the solid phase in gas–solid two-phase detonations) is considered as a special continuum, such that continuum mechanics can be employed to describe the bulk motion of the discrete phase. Then, the discrete phase becomes another "fluid", and the gaseous-phase flow and the discrete-phase flow can be solved by similar approaches. As for the Eulerian–Lagrangian framework, the gaseous phase is solved as in the Eulerian–Eulerian framework, but every discrete liquid particle (droplet) or solid particle is tracked individually by Newton's laws of motion.

In two-phase detonation modelling, it is a general way to assume that the particle (liquid or solid) of the discrete phase is small, spherical in shape and

uniformly suspended in the gas atmosphere. Additionally, the two-phase suspension is assumed to be diluted enough to neglect the volume fraction of discrete particles and particle–particle collisions. Two-phase detonation is a highly transient two-phase flow problem involving strong shock waves; hence, thermal and mechanical non-equilibrium between the gas and particles should be considered. Further, uniform distribution of temperature is considered within particles due to their small particle sizes, and ideally, all reaction heat is absorbed by gas only. Based on the above assumptions, the two-dimensional governing equation of the gaseous phase in an Eulerian–Eulerian framework can be expressed as follows [9]:

$$\frac{\partial U}{\partial t} + \frac{\partial F}{\partial x} + \frac{\partial G}{\partial y} = S + W, \tag{8.4}$$

where U is the vector of conserved variables, F and G the conservation flux vectors in the x- and y-directions, S the vector of two-phase interaction source terms, and W the vector of chemical reaction source terms, respectively. They can be expressed as

$$U = \begin{bmatrix} \rho_1 \\ \cdots \\ \rho_{ns} \\ \rho u \\ \rho v \\ E \end{bmatrix}, \quad F = \begin{bmatrix} \rho_1 u \\ \cdots \\ \rho_{ns} u \\ \rho u^2 + p \\ \rho u v \\ (E+p)u \end{bmatrix}, \quad G = \begin{bmatrix} \rho_1 v \\ \cdots \\ \rho_{ns} v \\ \rho u v \\ \rho v^2 + p \\ (E+p)v \end{bmatrix}, \quad W = \begin{bmatrix} \dot{\omega}_1 \\ \cdots \\ \dot{\omega}_{ns} \\ 0 \\ 0 \\ 0 \end{bmatrix}, \tag{8.5}$$

and

$$S = \begin{bmatrix} 0 \\ \vdots \\ J_p \\ \vdots \\ 0 \\ -f_x + u_p J_p \\ -f_y + v_p J_p \\ -q_p - (u_p f_x + v_p f_y) + (E_p/\rho_p) J_p \end{bmatrix}. \tag{8.6}$$

In the above equations, ρ_i is the mass density of species i and $i = 1, \ldots, ns$; ns is the number of species contained in the gas mixture; p, u, and v are the gas pressure and x- and y-components of gas velocity, respectively; $\dot{\omega}_i$ is the mass production rate of gaseous species i by chemical reactions; and ρ and E are the mass density and total energy per unit volume of the gas mixture, expressed as

$$\rho = \sum_{i=1}^{ns} \rho_i, \quad E = \rho h - p + \frac{1}{2}\rho(u^2 + v^2), \tag{8.7}$$

where h is the specific enthalpy of the gas mixture, calculated by

$$h = \sum_{i=1}^{ns} \frac{\rho_i}{\rho} h_i, \tag{8.8}$$

with the specific enthalpy of each individual species h_i as a function of gas temperature T, obtained from a species thermodynamic data base, such as the NASA Glenn data base [10]. By further assuming each species performs as a perfect gas, the equation of state of the gas mixture is then given by

$$p = \sum_{i=1}^{ns} \rho_i R_i T, \quad R_i = \frac{R_0}{W_i} \tag{8.9}$$

where $R_0 = 8.314 \, \text{J/(mol K)}$ is the universal gas constant, and W_i is the molar mass of species i. Variables in Eq. (8.6) are related to the properties of the discrete phase and the interaction between two phases. Their definitions will be given in the following paragraphs.

As for the discrete phase, the governing equation has a similar form as Eq. (8.4):

$$\frac{\partial U_p}{\partial t} + \frac{\partial F_p}{\partial x} + \frac{\partial G_p}{\partial y} = S_p, \tag{8.10}$$

where U_p, F_p and G_p are the vectors of conserved variables, conservation fluxes in the x- and y-directions of the discrete phase, which can be given by

$$U_p = \begin{bmatrix} \rho_p \\ \rho_p u_p \\ \rho_p v_p \\ E_p \\ N_p \end{bmatrix}, \quad F_p = \begin{bmatrix} \rho_p u_p \\ \rho_p u_p^2 \\ \rho_p u_p v_p \\ E_p u_p \\ N_p u_p \end{bmatrix}, \quad G_p = \begin{bmatrix} \rho_p v_p \\ \rho_p u_p v_p \\ \rho_p v_p^2 \\ E_p v_p \\ N_p v_p \end{bmatrix},$$

$$S_p = \begin{bmatrix} -J_p \\ f_x - u_p J_p \\ f_y - v_p J_p \\ q_p + (u_p f_x + v_p f_y) - (E_p/\rho_p) J_p \\ 0 \end{bmatrix} \tag{8.11}$$

In Eqs. (8.6) and (8.11), J_p is the mass regression rate (the combustion rate) of the discrete phase and it is determined by the combustion model of the discrete phase. ρ_p is the density of the discrete phase in the suspension. u_p and v_p are the x- and

y-components of the velocity of the discrete phase, respectively. E_p and N_p are the total energy per unit volume and the particle number density of the discrete phase, respectively. They can be calculated by

$$E_p = \rho_p e_p + \frac{1}{2}\rho_p(u_p^2 + v_p^2), \quad N_p = \frac{6\rho_p}{\pi\rho_m d_p^3}, \tag{8.12}$$

where e_p is the specific internal energy of the discrete phase and can also be obtained from a species thermodynamic data base as a function of discrete phase temperature T_p; d_p is the diameter of the particle; and ρ_m is the material density of the discrete phase.

Additionally, the x- and y-components of drag force acting on the discrete phase, f_x and f_y, can be modelled as follows:

$$\begin{cases} f_x = N_p\dfrac{\pi}{8}C_D d_p^2\rho|V - V_p|(u - u_p) \\ f_y = N_p\dfrac{\pi}{8}C_D d_p^2\rho|V - V_p|(v - v_p) \end{cases}, \tag{8.13}$$

where C_D is the drag coefficient,

$$C_D = \begin{cases} \frac{24}{\mathrm{Re}_p}\left(1 + \frac{1}{6}\mathrm{Re}_p^{2/3}\right), & \text{for } \mathrm{Re}_p < 1000 \\ 0.424, & \text{for } \mathrm{Re}_p \geq 1000 \end{cases}. \tag{8.14}$$

In Eqs. (8.13) and (8.14), the relative velocity and the relative Reynolds number Re_p between the gas and discrete phases can be calculated by

$$|V - V_p| = \left[(u - u_p)^2 + (v - v_p)^2\right]^{1/2}, \tag{8.15}$$

and

$$\mathrm{Re}_p = \frac{\rho d_p|V - V_p|}{\mu}, \tag{8.16}$$

where μ is the viscosity coefficient of gas. Accordingly, the convection heat transfer between the two phases is expressed as follows:

$$q_p = N_p\pi d_p\lambda\mathrm{Nu}_p(T - T_p), \tag{8.17}$$

with the two-phase Nusselt number expressed as functions of Re_p and Prandtl number Pr:

$$\mathrm{Nu}_p = 2 + 0.459\,\mathrm{Re}_p^{0.55}\,\mathrm{Pr}^{0.33}. \tag{8.18}$$

The CESE method has been proven to be of high accuracy and good stability in solving gaseous detonation problems in Sect. 8.1, and it is chosen to solve the two-phase detonation problems as well. That is, Eqs. (8.4) and (8.10) in the Eulerian–Eulerian framework can be solved using a CESE method, such as the a-α scheme. Theoretically, the source terms in the governing equations can be addressed together with the space–time integration in the CESE method [11–15]. However, a separated treatment of source terms is always employed in solving two-phase detonations, because the Jacobian matrixes of the interphase interaction and chemical reaction source terms in coupling treatment are rather complicated to calculate. Notably, with the source terms treated separately, it has been proven that the good accuracy and stability of the CESE method are preserved in high-speed reactive flow simulations [5, 16, 17]. On the other hand, the characteristic time scales of the interphase interaction and chemical reaction source terms are much smaller than that of flow dynamics, always leading to stiffness problems in two-phase detonation simulations. To overcome this problem, the operator-splitting technique with multiple sub-time steps [18] is always employed and then the source terms of interphase interactions and chemical reactions are explicitly integrated as ordinary differential equations. The detailed implementation process under the Eulerian–Eulerian framework can be illustrated as follows:

$$
\begin{cases}
\mathbf{U}_n \xrightarrow[\mathbf{S}=\mathbf{W}=0]{\text{CESE}} \widetilde{\mathbf{U}}_{n+1} \\
\mathbf{U}_p \xrightarrow[\mathbf{S}_p=0]{\text{CESE}} \widetilde{\mathbf{U}}_{p,n+1}
\end{cases}
\Rightarrow
\begin{cases}
\Delta t' = \Delta t/\text{N} \\
\mathbf{U}_{n+1}^{(0)} = \widetilde{\mathbf{U}}_{n+1} \\
\mathbf{U}_{p,n+1}^{(0)} = \widetilde{\mathbf{U}}_{p,n+1}
\end{cases}
$$

$$
\Rightarrow
\begin{cases}
\mathbf{U}_{n+1}^{(m)}, \mathbf{U}_{p,n+1}^{(m)} \to \mathbf{S}^{(m)}, \mathbf{W}^{(m)}, \mathbf{S}_p^{(m)} \\
\mathbf{U}_{n+1}^{(m+1)} = \mathbf{U}_{n+1}^{(m)} + \Delta t'[\mathbf{S}^{(m)} + \mathbf{W}^{(m)}] \\
\mathbf{U}_{p,n+1}^{(m+1)} = \mathbf{U}_{p,n+1}^{(m)} + \Delta t' \cdot \mathbf{S}_p^{(m)}
\end{cases}
$$

$$
\Rightarrow
\begin{cases}
\mathbf{U}_{n+1} = \mathbf{U}_{n+1}^{(N)} \\
\mathbf{U}_{p,n+1} = \mathbf{U}_{p,n+1}^{(N)}
\end{cases},
\tag{8.19}
$$

where the subscripts n and m refer to the global time step (Δt) and the sub-time step ($\Delta t'$), respectively, and N is the total number of sub-time steps within one global convection time step of the CESE method. Depending on the degree of stiffness in the problem, N can be chosen to be $10-20$.

To test the accuracy and robustness of the CESE method in two-phase detonation simulations under the Eulerian–Eulerian framework, Wang et al. [15] applied the CESE method to simulate the detonation synthesis of titania (TiO_2) nanoparticles. The corresponding chemical reaction can be described as follows:

$$
TiCl_4(g) + O_2(g) + 2H_2(g) \to TiO_2(s) + 4HCl(g)
\tag{8.20}
$$

As seen, it involves TiO_2 solid particles as well as $TiCl_4$, O_2, H_2 and HCl gases, implying that it is a gas–solid two-phase detonation problem. Simulation results showed that the simulated detonation profiles of gas density, pressure and temperature
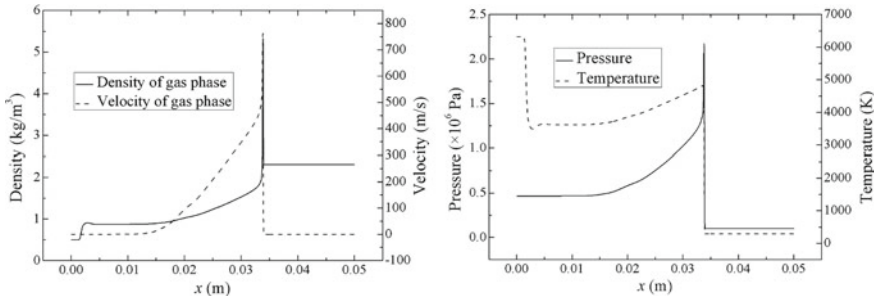
Fig. 8.8 Profiles of gas density, velocity, pressure and temperature in the detonation synthesis of nanosized TiO_2 particles. Courtesy of G. Wang [15]

are similar to those in the gaseous detonation wave, but a sudden drop of gas density can be captured after the detonation front because of phase transition from gas to solid particles, as shown in Fig. 8.8. Additionally, it is also found that the simulated particle size of the produced TiO_2 and the simulated peak pressure agreed well with other calculation and experiment data [19], respectively.

As for gas–liquid two-phase detonation, Wang et al. [3] solved the two-phase planar detonations of liquid hydrocarbon fuels with the same CESE method under the Eulerian–Eulerian framework. It is also found that the detonation profiles are similar to those of gaseous detonations, but with higher gas density, pressure and temperature behind the detonation front due to higher energy density of liquid fuels. Additionally, the length of the reaction zone is found to be longer as well, which is relative to the slower combustion rate of the liquid particle. Table 8.3 shows the comparisons of simulated detonation speeds to the experimental values. It can be revealed that the relative errors are less than 10% for particle sizes small than about 145 µm. As for two cases with larger particle sizes, the cases with relative errors exceeding 10%, it may be caused by the neglect of deformation of large liquid particles in modelling, since the combustion rate of liquid particle is influenced by particle deformation. All the above numerical results showed that that the CESE method is of high accuracy and good robustness in two-phase detonation simulations under an Eulerian–Eulerian framework.

The Eulerian–Eulerian framework is a simple and effective way to deal with the discrete phase in two-phase detonations, but it has some inherent limitations in modelling realistic two-phase suspension in industries or experiments with a specific particle size distribution, where a relatively wide range of particle diameters are involved [20–22]. Under the Eulerian–Eulerian framework, all particles within one numerical mesh are assumed to be in the same states, such as the same particle size, temperature, velocity and so on. However, the number of particles within one mesh may be large, and their states may differ depending on their initial states and interaction histories with gas phase. Moreover, the forces and the heat transfers between the gas and particles also differ by the particle size, resulting in different temperatures and

Table 8.3 Comparisons of detonation speeds of liquid hydrocarbon fuels between simulations and experiments. Courtesy of G. Wang [3]

Fuel	Particle size (μm)	Equivalence ratio	Experiment (m/s)	Simulation (m/s)	Relative error (%)
C_6H_{14}	20–30	0.41	1670	1544.83	−7.50
C_6H_{14}	20–30	0.49	1720	1671.30	−2.83
C_6H_{14}	20–30	0.56	1700	1773.92	4.35
C_6H_{14}	20–30	0.68	1780	1935.89	8.76
$C_{10}H_{20}$	145	1.0	2130	1946.93	−8.59
$C_{10}H_{20}$	375	0.914	1810–1850	1996.72	7.93–10.32
$C_{10}H_{20}$	1300	0.23	970–1250	1169.97	−6.40–20.62

velocities of particles within one computational mesh. Further, it had been demonstrated that many two-phase detonation characteristics are significantly influenced by the particle size. Consequently, the Eulerian–Eulerian framework is insufficient to reflect the true physics of realistic two-phase detonations with particle size distributions and to simulate them accurately, which raises the demand of modelling realistic two-phase detonation under the Eulerian–Lagrangian framework where the discrete particles are tracked individually.

Under the Eulerian–Lagrangian framework, Eq. (8.4) is still applied as the governing equation of the gas phase, and **U**, **F**, **G** and **W** have the same forms as Eq. (8.5). However, the two-phase interaction source term **S** is expressed in the following form instead,

$$\mathbf{S} = \frac{1}{dV} \sum_{k=1}^{np} \begin{bmatrix} 0 \\ \vdots \\ J_{pk} \\ \vdots \\ 0 \\ -f_{xk} + u_{pk} J_{pk} \\ -f_{yk} + v_{pk} J_{pk} \\ -q_{pk} - \left(u_{pk} f_{xk} + v_{pk} f_{yk} \right) + \frac{1}{2} \left(u_{pk}^2 + v_{pk}^2 \right) \cdot J_{pk} + e_{pk} \cdot J_{pk} \end{bmatrix}, \tag{8.21}$$

where subscript k represents all the quantities related to the kth particle (solid or liquid). To include all effects of particles into the source term **S** of the gaseous equation, the summation is done within the gaseous mesh element dV, and np is the number of particles in dV.

The motion of every particle is then descripted using Newton's laws of motion instead of the Eulerian form Eq. (8.10). For the kth particle, the corresponding governing equation can be written as

$$\frac{d\mathbf{L}_{pk}}{dt} = \mathbf{S}_{pk}, \tag{8.22}$$

where $\mathbf{L}_{pk}$ and $\mathbf{S}_{pk}$ are the vectors of the Lagrangian variables of the kth particle and the corresponding source terms, respectively, and they are expressed as

$$\mathbf{L}_{pk} = \left[m_{pk}, x_{pk}, y_{pk}, m_{pk}u_{pk}, m_{pk}v_{pk}, E_{pk}\right]^{\mathrm{T}}, \tag{8.23}$$

and

$$\mathbf{S}_{pk} = \left[-J_{pk}, u_{pk}, v_{pk}, f_{xk}, f_{yk}, -e_{pk}J_{pk} + q_{pk}\right]^{\mathrm{T}}. \tag{8.24}$$

In Eq. (8.23), m_{pk} and E_{pk} are the mass and total internal energy of the kth particle, respectively, and $E_{pk} = m_{pk}{\cdot}e_{pk}$.

Further, the Lagrangian forms of the drag force and the convection heat of the kth particle can be easily derived from the according Eulerian forms Eqs. (8.13) and (8.17), as follows:

$$\begin{cases} f_{xk} = \dfrac{\pi}{8}C_{Dk}d_{pk}^2\rho\left|V - V_{pk}\right|(u - u_{pk}) \\ f_{yk} = \dfrac{\pi}{8}C_{Dk}d_{pk}^2\rho\left|V - V_{pk}\right|(v - v_{pk}) \end{cases}, \tag{8.25}$$

and

$$q_{pk} = \pi d_{pk}\lambda \mathrm{Nu}_{pk}\left(T - T_{pk}\right). \tag{8.26}$$

Under the Eulerian–Lagrangian framework, the CESE method is again applied to solve the gas phase equation, while the source terms of interphase interactions and chemical reactions are treated separately and integrated explicitly as ordinary differential equations, along with the integration of particle Lagrangian equations, by using the operator-splitting technique as well, as depicted below,

$$\mathbf{U}_n \xrightarrow[\mathbf{S}=\mathbf{W}=0]{\mathrm{CESE}} \tilde{\mathbf{U}}_{n+1} \Rightarrow \begin{cases} \Delta t' = \Delta t/N \\ \mathbf{U}_{n+1}^{(0)} = \tilde{\mathbf{U}}_{n+1} \\ \mathbf{L}_{pk,n+1}^{(0)} = \mathbf{L}_{pk,n} \end{cases}$$

$$\Rightarrow \begin{cases} \mathbf{U}_{n+1}^{(m)}, \mathbf{L}_{pk,n+1}^{(m)} \to \mathbf{S}^{(m)}, \mathbf{W}^{(m)}, \mathbf{S}_{pk}^{(m)} \\ \mathbf{U}_{n+1}^{(m+1)} = \mathbf{U}_{n+1}^{(m)} + \Delta t'[\mathbf{S}^{(m)} + \mathbf{W}^{(m)}] \\ \mathbf{L}_{pk,n+1}^{(m+1)} = \mathbf{L}_{pk,n+1}^{(m)} + \Delta t' \cdot \mathbf{S}_{pk}^{(m)} \end{cases}$$

$$\Rightarrow \begin{cases} \mathbf{U}_{n+1} = \mathbf{U}_{n+1}^{(N)} \\ \mathbf{L}_{pk,n+1} = \mathbf{L}_{pk,n+1}^{(N)} \end{cases}. \tag{8.27}$$

Notably, the Eulerian–Lagrangian framework had rarely been developed to solve high-speed reactive two-phase flows, mainly because the number of fine particles has proven too large and simulations too expensive to achieve in the past. Nowadays, with the rapid development of computer technologies, parallel computation techniques such as the Message Passing Interface (MPI) technique may help to make simulations of two-phase detonations with fine particles under an Eulerian–Lagrangian framework possible. However, the application of MPI parallel computation technique to an Eulerian–Lagrangian framework is not as straightforward as that under a purely Eulerian framework. A large amount of information exchange from one computational core to another is needed for calculations of the interaction source terms between two phases, leading to formidable communication cost even exceeding the computational cost, especially when the Eulerian framework is staggered with the Lagrangian framework due to the relative movement between these two phases.

To solve the communication problem of parallel computing technique of high-speed two-phase flows under an Eulerian–Lagrangian framework, the traditional static data structure, such as multi-dimensional array, should be avoided using to store the information of the discrete phase described under the Lagrangian framework. Notably, the order of particles presented under the Lagrangian framework is not important and does not need to be preserved as its initial order. The only operation required for coding is to traverse every particle one by one. Inspired by the above facts, dynamic data structures can be introduced to store particle information and solve the communication problem under the Eulerian–Lagrangian framework. For example, the structures and the corresponding operations of linked lists used to store particle information are schematically shown in Fig. 8.9. As seen, each CPU owns one linked list to store information of the particles that are at the corresponding locations to the gas phase. In each linked list, one node represents one particle and consists of two parts: the data part that stores particle information, and the pointer that points to the next node of the particle for traversing. The pointer of the last node always points to the "NULL", implying that the linked list has ended.

Additionally, there are four basic operations for the linked list to adjust the particle's storage location: allocate, free, delete and insert, as depicted in Fig. 8.9. The "allocate" operation is used to allocate new memory to store information about a "new" particle, the "free" operation to free the memory that stores information about an "old" particle, the "delete" operation to disconnect one particle from the linked list, and the "insert" operation to connect one particle at the end of the linked list. When the particle phase is staggered with the gas phase because of relative motion, the information of the particles, whose locations exceed the corresponding location ranges assigned to the present CPUs, will be transferred to and stored in the CPUs with the correct particle location ranges. For example, for CPU A in Fig. 8.9, where one particle is removed, the following sequence of operations is needed:

(1) send the information of the specific particle to CPU B;
(2) delete the particle node from the linked list;
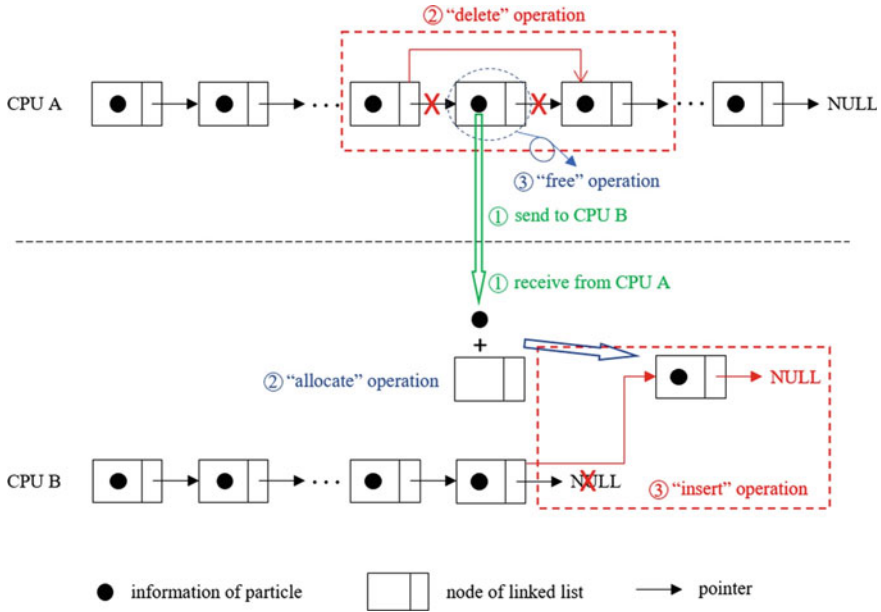(3) free the memory of the separated node.

Fig. 8.9 Linked lists and operation sequences. Courtesy of Z. J. Zhang [9]

Meanwhile, for CPU B in Fig. 8.9, where a new particle is received, the corresponding operation sequence is:

(1) receive the information of the new particle from CPU A;
(2) allocate a new node and store the information into the data field of the node;
(3) insert the new particle node at the end of the linked list.

With this dynamic data structure and the corresponding operation sequences, the information about Lagrangian particles is always stored in the CPUs of the correct Eulerian coordinates, and therefore excessive communication between CPUs when calculating gas-particle interactions is avoided, as shown in Fig. 8.10. Moreover, with the limitation of the global time step by the CFL condition, only "one" particle at most will cross the CPU boundary at every iteration; that is, the information of "one" particle at most will be transferred to the other CPU at one iteration step by the above operation sequence. As a result, the communication cost of the MPI parallel for the gas-particle interaction calculation will be reduced from O(N) to O(1) when using this data structure. Here, N is the number of particles stored in each CPU.

To demonstrate the MPI parallelization performance with the use of the above linked lists and the corresponding operation sequences, Fig. 8.11 depicts the speedup parameters of a 2D Al-air detonation propagation problem using the CESE method under an Eulerian–Lagrangian framework, which involves approximately 24 million Eulerian meshes and about 75 million Lagrangian particles in the computational domain. This test case is simulated on the Tianhe-2 supercomputer from China with core numbers of 1, 2, 3, 4, 6, 12, 24, 48, 96, 192 and 384. The use of one core means
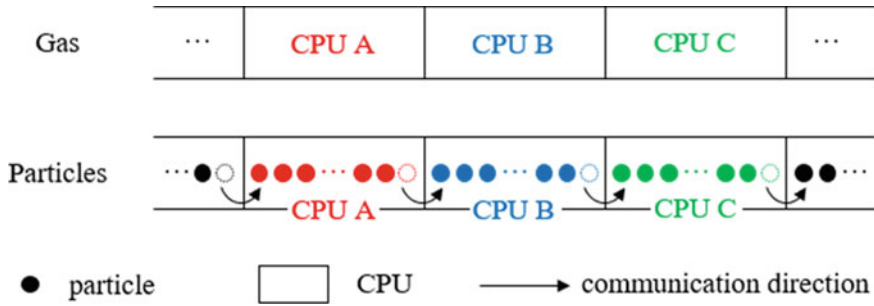
Fig. 8.10 Dynamic data structure using the linked list in the Eulerian–Lagrangian framework. Courtesy of Z. J. Zhang [9]

that the simulation is done serially. As depicted in Fig. 8.11, when 384 cores are used, the code using linked lists still has a reasonable parallel efficiency of about 50% for the tested problem, while MPI parallelization under the Eulerian–Lagrangian framework using multi-dimensional static arrays is impossible, even with only 2 cores, as the communication cost is shown to be unacceptably large. This means that the linked list dynamic data structure works well in the MPI implement when solving two-phase detonations under the Eulerian–Lagrangian framework.

To test the performances of CESE method in simulations of two-phase detonation under the Eulerian–Lagrangian framework, Shen et al. [23] simulated the gas–liquid two-phase detonations in the $C_{10}H_{22}$–O_2/air systems with different fuel droplet sizes and equivalence ratios. A deficit in the detonation speed compared to the corresponding purely gaseous one was observed in the gas–liquid suspensions with lean fuel and larger droplet sizes, while an increase in the detonation speed was observed

Fig. 8.11 Speedups of the tested problem using linked lists. Courtesy of Z. J. Zhang [9]
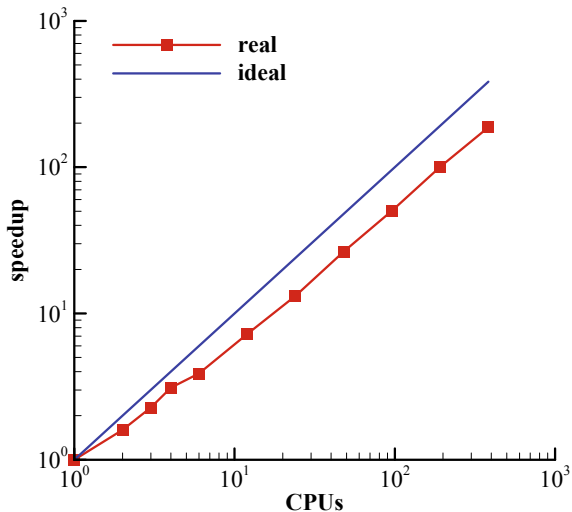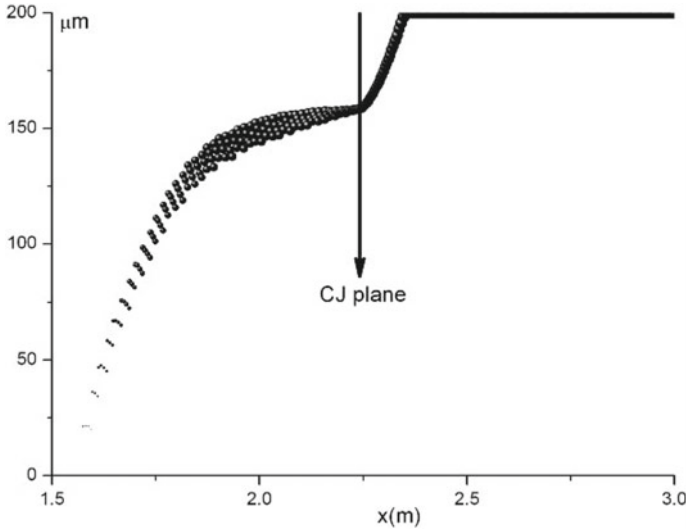
Fig. 8.12 Distribution of particle size near the detonation front in gas–liquid two-phase detonations. Courtesy of H. Shen [23]

with very rich fuel. This special two-phase detonation feature in rich fuel is due to the slow combustion rate of the droplet, leading to a large amount of fuel burnt behind the C–J point, as shown in Fig. 8.12. As a result, the efficient equivalence ratio is reduced and detonation speed shifts to the equivalence ratio direction. The accuracy and robustness of the CESE method applied to two-phase detonation simulations under an Eulerian–Lagrangian framework had been demonstrated.

Notably, simulations of the monodisperse two-phase detonation problems (with single particle size) under the Eulerian–Lagrangian framework always present the same results as those performed under the Eulerian–Eulerian framework. The raising of modelling two-phase detonations under the Eulerian–Lagrangian framework is in fact to simulate the realistic polydisperse two-phase detonations, where a particle size distribution is involved and the particle diameters are in a relatively wide range. One of the frequently used particle size distribution models to describe the polydisperse suspension is the log-normal distribution function, expressed by the number frequency distribution function as follows [24]:

$$f_n\left(d_p\right) = \frac{1}{\sqrt{2\pi}\,\sigma_0} \exp\left[-\frac{1}{2}\left(\frac{\ln d_p - \ln d_{nM}}{\sigma_0}\right)^2\right]\frac{1}{d_p}, \qquad (8.28)$$

where d_{nM} and σ_0 are the number median diameter and standard deviation of the distribution, respectively. In practice, the specific particle size distribution of a polydisperse suspension is always given by other two particle size parameters that can be

easily measured, namely the volume-average diameter ($\bar{d}$) and the mass-weighted-average particle diameter ($\bar{d}_m$). For example, the measured polydisperse parameters of the Al powder tested in the experiment of Zhang et al. [20] are $\bar{d} = 2\,\mu$m and $\bar{d}_m = 3.3\,\mu$m. The relationships between (d_{nM}, σ_0) and ($\bar{d}, \bar{d}_m$) can be obtained through the integrations of Eq. (8.28), as follows

$$
\begin{cases}
\bar{d} = \left[\displaystyle\int_0^\infty s^3 f_n(s)ds \right]^{1/3} = d_{nM}e^{\frac{3}{2}\sigma_0^2} \\
\bar{d}_m = \left[\displaystyle\int_0^\infty s^4 f_n(s)ds \right] \Big/ \left[\displaystyle\int_0^\infty s^3 f_n(s)ds \right] = d_{nM}e^{\frac{7}{2}\sigma_0^2}
\end{cases}
\tag{8.29}
$$

Consequently, the corresponding parameters of the above-mentioned Al powder are $d_{nM} = 1.37\,\mu$m and $\sigma_0 = 0.5$. However, it is a good way to use the parameter set of ($\bar{d}, \sigma_0$) to discuss the polydisperse suspensions in numerical simulations, because the effects of particle size distribution on polydisperse detonations can be easily discussed by varying σ_0. Some specific particle size distributions with fixed $\bar{d} = 2\,\mu$m and different σ_0 values are depicted in Fig. 8.13.

In the followings, the typical Al-Air detonation problems with different particle size distributions, taking as an example, are simulated by the above numerical algorithm under the Eulerian–Lagrangian framework, to show the capacities of the CESE method in solving polydisperse two-phase detonation and show the differences between monodisperse and polydisperse two-phase detonations. The single-step global chemical reaction occurs in the Al-air suspension is
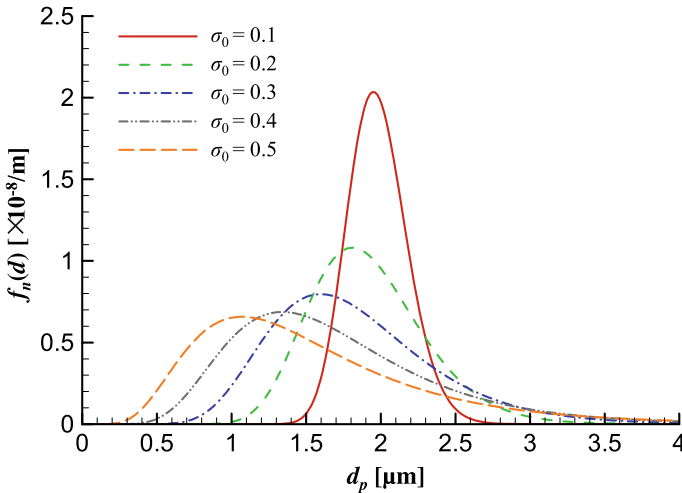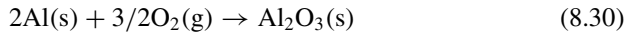
$$
2\mathrm{Al(s)} + 3/2\mathrm{O}_2(\mathrm{g}) \rightarrow \mathrm{Al}_2\mathrm{O}_3(\mathrm{s})
\tag{8.30}
$$

Fig. 8.13 Log-normal particle size distributions with $\bar{d} = 2\,\mu$m. Courtesy of Z. J. Zhang [25]

To model the combustion rate of every single Al particle, the surface-kinetic-oxidation and diffusion hybrid combustion model (originally proposed by Zhang et al. [26]) can be employed. The Lagrangian form of the combustion rate of the kth Al particle is given as

$$J_{pk,\text{Al}} = \pi d_{pk,\text{Al}}^2 C_{O_2} \frac{\nu_{\text{Al}} W_{\text{Al}}}{\nu_{O_2} W_{O_2}} \cdot \frac{k_{dk} k_{sk}}{k_{dk} + k_{sk}}. \tag{8.31}$$

where the reaction rates for the diffusion-controlled and kinetic-controlled combustion regime are expressed by

$$\begin{cases} k_{dk} = \dfrac{\nu_{O_2} W_{O_2}}{\nu_{\text{Al}} W_{\text{Al}}} \dfrac{\rho_{\text{Al}} d_{pk,\text{Al}}}{2 C_{\text{total}} K d_{pk0,\text{Al}}^2} \left(1 + 0.276 \text{Re}_{pk}^{1/2} \text{Pr}^{1/3} \right). \\ k_{sk} = k_0 e^{-E_a/R_0 T_{sk}} \end{cases} \tag{8.32}$$

In Eqs. (8.31) and (8.32), ν_{Al} and ν_{O_2} are the stoichiometric coefficients for Al and O_2, respectively; C_{O_2} and C_{total} are the mole concentrations of O_2 and gas mixture, respectively; T_{sk} is the particle surface temperature; and K, k_0 and E_a are model constants.

As depicted in Fig. 8.14. Some special two-phase detonation features corresponding to multi-phase interaction can be clearly identified in the detonation front structures of monodisperse Al-air detonation. The first feature is known as "double peaks" in the gas pressure, density and velocity profiles (Fig. 8.14a, c), which is distinctly different from the single peak feature observed in gaseous detonations. It is demonstrated, from the one-dimensional flow theory in gas dynamics that the second peak in the detonation front structures of monodisperse Al suspension is caused by the dominant stage of heat transfer due to intense phase transition (Al evaporation) at a specific location after the shock front. The second feature, shown in Fig. 8.14b, is the plateau of particle temperature due to Al evaporation, which is equal to 2750 K and results in the observed "kink" in the gas temperature profile due to the intense heat transfer between the gas and particles. The third feature, shown in Fig. 8.14c, is the particle velocity lag in the velocity relaxation process, resulting in the alternative forces acting on particles and momentum transfers between the gas and particles. All these two-phase features for monodisperse Al-air detonation are similar with those obtained by Zhang et al. [26] and Teng and Jiang [27, 28].

However, as for the polydisperse detonation with a log-normal particle size distribution of $\sigma_0 = 0.5$, most features of monodisperse Al detonation, including the double peaks in gas pressure, density, velocity profiles and the kink in gas temperature profile, disappear, and only single peaks of gas quantities exist in the detonation front, which are quite similar to the wave front structures in gaseous detonations. The double peaks in the detonation front is demonstrated theoretically to be attributed to the space-dispersed phase transition processes of particles of different sizes result in an overall moderate heat transfer intensity, which hinders the formation of the heat-transfer-dominant stage. These differences between monodisperse and polydisperse
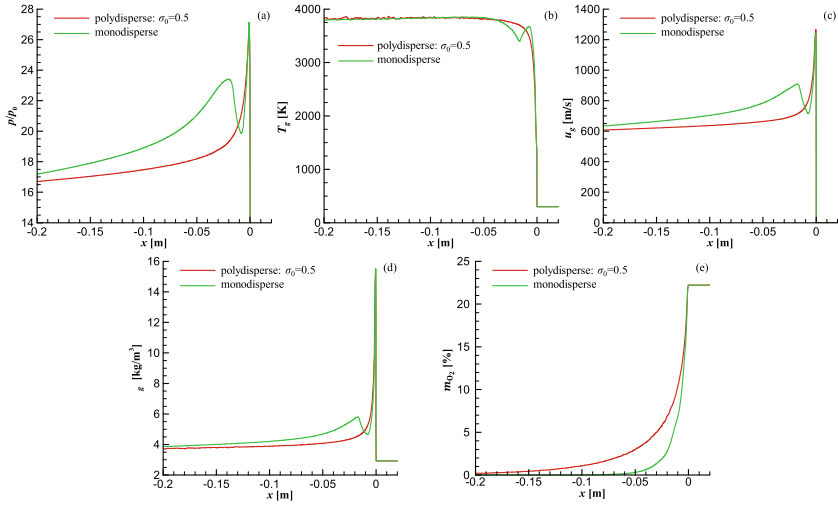
Fig. 8.14 Comparison of front structures in gas phase of polydisperse and monodisperse Al-air detonations: **a** pressure, **b** temperature, **c** velocity, **d** density, **e** mass fraction of O_2. Courtesy of Z. J. Zhang [25]

two-phase detonations are relative to the multiple timescales and length scales in polydisperse suspension with a continuous particle size distribution.

As for the multi-dimensional two-phase detonation features, Fig. 8.15 shows the comparisons of cellular detonation flow fields between monodisperse and polydisperse detonations. As indicated in Fig. 8.15a, typical cellular detonation structures, including pairs of triple points, Mach stems, incident shock waves and pairs of transverse waves, can be observed in both the monodisperse and polydisperse detonation fronts. Moreover, the gas temperature and the O_2 species mass fraction distributions for both monodisperse and polydisperse cases are non-uniform behind the detonation fronts, which are characterized by irregular local (high and low) temperature and O_2 concentration zones, respectively, as shown in Fig. 8.15b, c. These irregular distributions of the flow field parameters in monodisperse and polydisperse detonations are both caused by the periodical motions of triple points along the detonation fronts. All these features in two-phase detonations are similar to those observed in gaseous detonations, except for the transverse waves. The transverse waves in both the monodisperse and polydisperse detonation fronts are weak and degenerate fairly fast in the rear flows, which are different from the strong transverse waves observed in purely gaseous detonations. According to Zhang et al. [26], these weak transverse waves can be attributed to the slow diffusion-controlled combustion of the majority of Al particles after their kinetic-inductions and a considerable amount of condensed Al oxide formed in the detonation products without contributing to gas pressure.
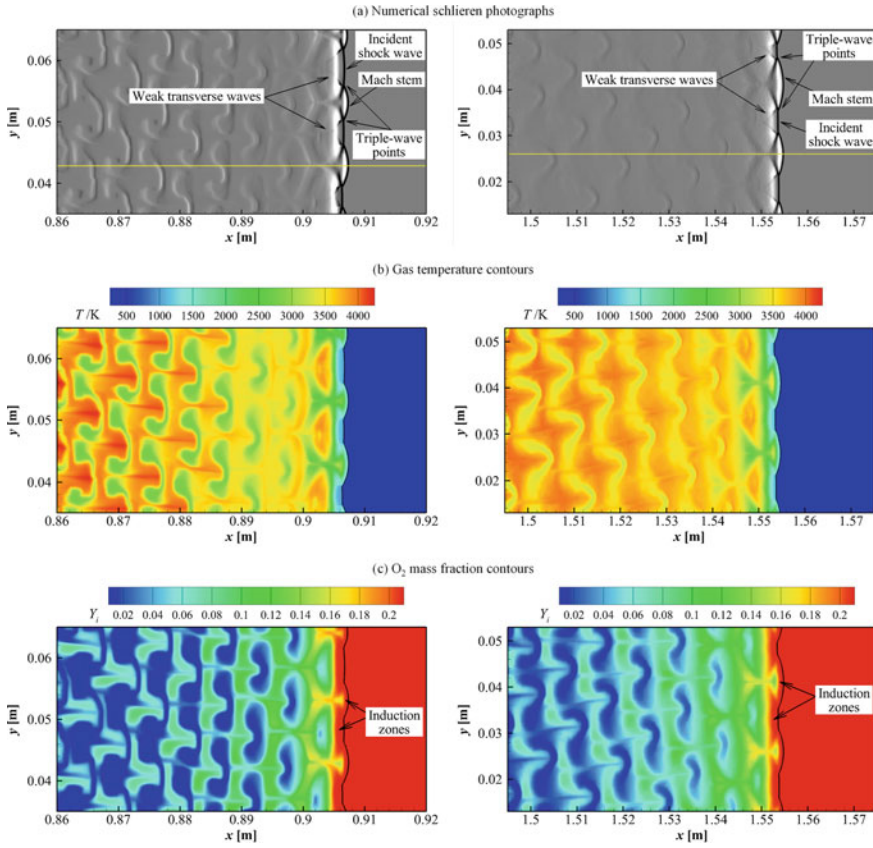
Fig. 8.15 Comparison of flow fields in Al-air detonation fronts. Left: monodisperse with $d_p = 2\,\mu$m at $t = 0.6$ ms. Right: polydisperse with $\overline{d} = 2\,\mu$m and $\sigma_0 = 0.5$ at $t = 1$ ms. Courtesy of Z. J. Zhang [25]

Further, larger detonation cell sizes are expected in polydisperse two-phase deto-nation compared to monodisperse detonation, since the reaction zone is larger, as shown in Fig. 8.16 by peak pressure contours. The estimated cell sizes of the monodis-perse detonation and the polydisperse detonations ($\sigma_0 = 0.5$ and 0.8) are $\lambda_{\text{monodisperse}} = 10.5 \pm 0.5$ mm, $\lambda_{0.5} = 13.3 \pm 0.8$ mm and $\lambda_{0.8} = 20.0 \pm 1.8$ mm, respectively. $\lambda_{0.5}$ is 27% larger than $\lambda_{\text{monodisperse}}$, and $\lambda_{0.8}$ is even 190% larger. Figure 8.17 plots these detonation cell sizes as a function of the square of standard deviation σ_0^2 by a logarithmic scatter diagram, together with those of other three polydisperse detona-tions with different σ_0. An approximately linear relationship between $\ln\lambda$ and σ_0^2 can be captured. Then, linear fitting is employed, and the fitting function appears to be $\ln\lambda = 0.9367\sigma_0^2 + 0.0655$, implying that the detonation cell size λ of polydis-perse suspensions is an exponent function of the square of standard deviation of the distribution σ_0^2. This is an important quantitative relation of polydisperse two-phase
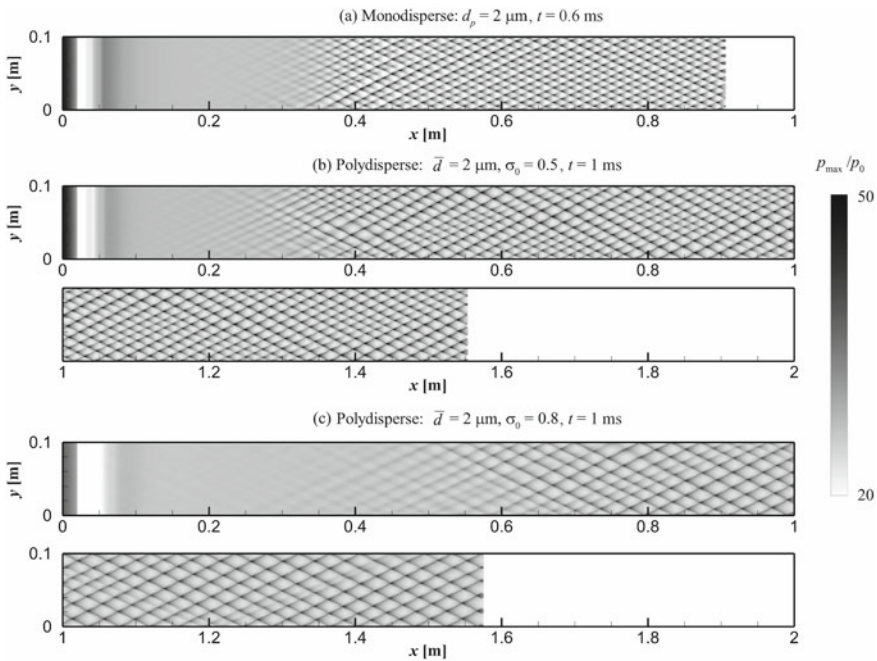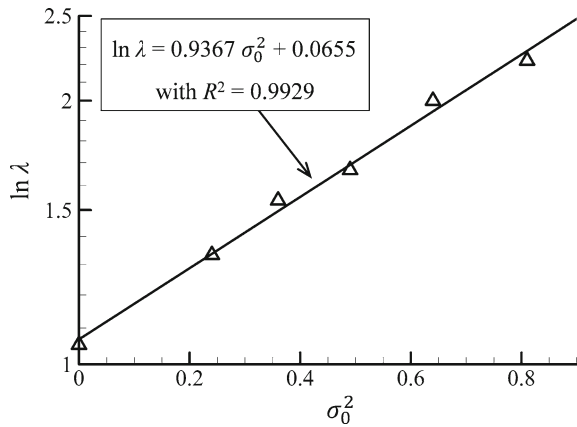
Fig. 8.16 Comparison of cellular detonations (peak pressure contours) of Al-air mixtures: **a** monodisperse with $d_p = 2\ \mu$m, **b** polydisperse with $\bar{d} = 2\ \mu$m and $\sigma_0 = 0.5$, and **c** polydisperse with $\bar{d} = 2\ \mu$m and $\sigma_0 = 0.8$. Courtesy of Z. J. Zhang [25]

Fig. 8.17 Detonation cell size λ of Al-air suspension as a function of square of standard deviation σ_0^2

$$\ln \lambda = 0.9367\ \sigma_0^2 + 0.0655$$

with $R^2 = 0.9929$

detonation to evaluate the effect of particle size distribution on detonation cell size. From the above results, the capacities of the CESE method in polydisperse two-phase detonation simulations under the Eulerian–Lagrangian framework is demonstrated as well.

References

1. Shen, H., & Parsani, M. (2017). The role of multidimensional instabilities in direct initiation of gaseous detonations in free space. *Journal of Fluid Mechanics, 813*, R4.
2. Shi, L. S., Uy, K. C. K., & Wen, C. Y. (2020). The re-initiation mechanism of detonation diffraction in a weakly unstable gaseous mixture. *Journal of Fluid Mechanics, 895*, A24.
3. Wang, G., Zhang, D. L., Liu, K. X., & Wang, J. T. (2010). An improved CE/SE scheme for numerical simulation of gaseous and two-phase detonations. *Computers & Fluids, 39*(1), 168–177.
4. Shen, H., Liu, K. X., & Zhang, D. L. (2011). Three-dimensional simulation of detonation propagation in a rectangular duct by an improved CE/SE scheme. *Chinese Physics Letters, 28*(12), 124705.
5. Shi, L. S., Shen, H., Zhang, P., Zhang, D. L., & Wen, C. Y. (2017). Assessment of vibrational non-equilibrium effect on detonation cell size. *Combustion Science and Technology, 189*(5), 841–853.
6. Uy, K. C. K., Shi, L. S., & Wen, C. Y. (2020). Numerical analysis of the vibration-chemistry coupling effect on one-dimensional detonation stability. *Aerospace Science and Technology, 107*, 106327.
7. Uy, K. C. K., Shi, L. S., Hao, J., & Wen, C. Y. (2020). Linear stability analysis of one-dimensional detonation coupled with vibrational relaxation. *Physics of Fluids, 32*(12), 126101.
8. Wang, F., Weng, C. S., Wu, Y. W., Bai, Q. D., Zheng, Q., & Xu, H. (2020). Numerical research on kerosene/air rotating detonation engines under different injection total temperatures. *Aerospace Science and Technology, 103*, 105899.
9. Zhang, Z., Wen, C. Y., Liu, Y., Zhang, D. L., & Jiang, Z. (2019). Application of CE/SE method to gas-particle two-phase detonations under an Eulerian-Lagrangian framework. *Journal of Computational Physics, 394*, 18–40.
10. McBride, B. J. (2002). *NASA Glenn coefficients for calculating thermodynamic properties of individual species*. National Aeronautics and Space Administration, John H. Glenn Research Center.
11. Yu, S. T., Chang, S. C., Yu, S. T., & Chang, S. C. (1997). Treatments of stiff source terms in conservation laws by the method of space-time conservation element/solution element. In *35th Aerospace Sciences Meeting and Exhibit*.
12. Park, S. J., Yu, S. T., Lai, M. C., Chang, S. C., & Jorgenson, C. (1999). Numerical calculation of unstable detonations by the method of space-time conservation element and solution element. In *37th Aerospace Sciences Meeting and Exhibit*.
13. Wang, B., He, H., & Yu, S. T. J. (2005). Direct calculation of wave implosion for detonation initiation. *AIAA Journal, 43*(10), 2157–2169.
14. Wang, J. T., Liu, K. X., & Zhang, D. L. (2009). An improved CE/SE scheme for multi-material elastic–plastic flows and its applications. *Computers & Fluids, 38*(3), 544–551.
15. Wang, G., Zhu, H. Y., Sun, Q. H., Zhang, D. L., & Liu, K. X. (2011). An improved CE/SE scheme and its application to dilute gas–particle flows. *Computer Physics Communications, 182*(8), 1589–1601.
16. Wen, C. Y., Saldívar Massimi, H., & Shen, H. (2018). Extension of CE/SE method to non-equilibrium dissociating flows. *Journal of Computational Physics, 356*, 240–260.
17. Uy, K. C. K., Shi, L. S., & Wen, C. Y. (2019). Prediction of half reaction length for H_2–O_2-Ar detonation with an extended vibrational nonequilibrium Zel'dovich−von Neumann−Döring (ZND) model. *International Journal of Hydrogen Energy, 44*(14), 7667–7674.
18. Ropp, D. L., & Shadid, J. N. (2009). Stability of operator splitting methods for systems with indefinite operators: Advection–diffusion–reaction systems. *Journal of Computational Physics, 228*(9), 3508–3516.
19. Ouyang, X., Li, X., Yan, H., Mo, F., & Zhao, C. (2008). Preparation and characterization of nanosized TiO_2 powders by gaseous detonation method. *Materials Science and Engineering: B, 153*(1–3), 21–24.

20. Zhang, F., Murray, S., & Gerrard, K. (2006). Aluminum particles-air detonation at elevated pressures. *Shock Waves, 15*(5), 313–324.
21. Zhang, F., Gerrard, K., & Ripley, R. C. (2009). Reaction mechanism of aluminum-particle-air detonation. *Journal of propulsion and power, 25*(4), 845–858.
22. Meda, L., Marra, G., Galfetti, L., Severini, F., & De Luca, L. (2007). Nano-aluminum as energetic material for rocket propellants. *Materials Science and Engineering: C, 27*(5–8), 1393–1396.
23. Shen, H., Wang, G., Liu, K. X., & Zhang, D. L. (2012). Numerical simulation of liquid-fueled detonations by an Eulerian-Lagrangian model. *International Journal of Nonlinear Sciences and Numerical Simulation, 13*(2), 177–188.
24. Crowe, C., Schwarzkopf, J., Sommerfeld, M., & Tsuji, Y. (2011). Multiphase flows with droplets and particles. CRC Press.
25. Zhang, Z., Wen, C. Y., Liu, Y., Zhang, D. L., & Jiang, Z. (2020). Effects of different particle size distributions on aluminum particle–air detonation. *AIAA Journal, 58*(7), 3115–3128.
26. Zhang, F. (2009). Detonation of gas-particle flow. In *Shock wave science and technology reference library* (Vol. 4, pp. 87–168). Springer.
27. Teng, H., & Jiang, Z. (2013). Effects of different product phases in aluminum dust detonation modeling. *Science China Physics, Mechanics and Astronomy, 56*(11), 2178–2185.
28. Teng, H., & Jiang, Z. (2013). Numerical simulation of one-dimensional aluminum particle-air detonation with realistic heat capacities. *Combustion and Flame, 160*(2), 463–472.